Electronic Supporting Information

Water-Soluble Nickel and Iron Salt Precatalysts for Hydroxymethylfurfural (HMF) and Water Oxidation†

Till Kahlstorf,‡[a] J. Niklas Hausmann,‡*[a] Indranil Mondal[b], Konstantin Laun[c], Ingo Zebger[c] and Prashanth W. Menezes*[a,b]

Till Kahlstorf, J. N. Hausmann, Prashanth W. Menezes
Material Chemistry Group for Thin Film Catalysis–CatLab
Helmholtz-Zentrum Berlin für Materialien und Energie
Albert-Einstein-Str. 15, 12489 Berlin, Germany
E-mail: prashanth.menezes@helmholtz-berlin.de, niklas.hausmann@helmholtz-berlin.de

Indranil Mondal, Prashanth W. Menezes
Department of Chemistry: Metalorganics and Inorganic Materials,
Technische Universität Berlin,
Straße des 17 Juni 135, Sekr. C2, 10623 Berlin, Germany.
E-mail: prashanth.menezes@mailbox.tu-berlin.de

Konstantin Laun, Ingo Zebger
Department of Chemistry, Physical Chemistry/Biophysical Chemistry
Technische Universität Berlin,
Straße des 17. Juni 135, Sekr. PC14, 10623 Berlin, Germany
Email: ingo.zebger@tu-berlin.de

‡ These authors contributed equally to this work.

Experimental

Chemicals and Materials

Carbon cloth: CC, CeTech W0S1002, thickness = 0.36 mm, basic 15 weight = 120 g cm^{-2}, sheet resistance = 0.60 Ω sq^{-1}, before using the carbon cloth it was cleaned by acid treatment in 36 % HNO_3 at 90 °C under reflux for 24 hours, washed with water and ethanol and then dried.

Ethanol: Fischer Chemical 99.8 %

1 M aqueous KOH: Alfa Aesar 1.0 N standardised solution, Fe content from ICP <0.05 ppm

Nickel(II) nitrate hexahydrate: Sigma Aldrich 99.999 % trace metal basis

Iron(III) nitrate nonahydrate: Sigma Aldrich, 99.95 %

5-Hydroxymethyl-2-furaldehyde: Alfa Aesar, 97 %

milli-Q® water: 18.2 MΩ·cm

Drop Coating of the Electrodes

Drop coating of nickel nitrate on carbon cloth (NiNO$_3$-CC). Typically, 1.00 g of $Ni(NO_2)_3 \cdot 6\ H_2O$ (3.43 mmol) were dissolved in 20 ml ethanol, yielding a concentration of 50.0 mg ml^{-1} (0.172 mM) or 10.1 mg ml^{-1} (0.172 mM) with respect to nickel. For the 2 mg nickel loading, 198 µl were drop coated on activated carbon cloth substrates (geometrical surface area 1 cm^2) using an Eppendorf pipette in four 49.5 µl steps. The samples were subsequently dried in air at room temperature. Carbon cloths treated this way are subsequently called NiNO$_3$-CC. After the sample activation described on the next page, they are called NiNO$_3$-CC-OER.

Drop coating of nickel and iron nitrate on carbon cloth (NiFeNO$_3$-CC). Analogous to the NiNO$_3$-CC electrodes, 800 mg of $Ni(NO_3)_2 \cdot 6\ H_2O$ (2.75 mmol) and 290 mg $Fe(NO_3)_3 \cdot 9\ H_2O$ (0.718 mmol) were dissolved in 20 ml ethanol to achieve an iron content of 20 % (the Ni:Fe ratio is 4:1). The drop coating was carried out identically to $Ni(NO_3)_2$, yielding a metal loading of 2 mg. Carbon cloths treated this way are subsequently called NiFeNO$_3$-CC. After the sample activation described on the next page, they are called NiFeNO$_3$-CC-OER.

Electrochemistry

Electrochemical measurements

A standard three-electrode (working, counter, and reference) electrochemical cell with 15 ml 1.0 M aqueous KOH (pH 13.89)[1] and a potentiostat (SP-200, BioLogic Science Instruments) controlled by the EC-Lab v10.20 software package was utilised for the measurements. Activated $Ni(NO_3)_2$ and $NiFe(NO_3)_x$ carbon cloth supported electrodes (termed $NiNO_3$-CC-OER / $NiFeNO_3$-CC-OER) were used as the working, Pt wire (0.5 mm diameter × 230 mm length, A-002234, BioLogic) as the counter electrode, and Hg/HgO (CH Instruments, Inc.) as the reference electrode. The Hg/HgO potentials were referenced to the reversible hydrogen electrode (RHE) through calibration with a self-made RHE.[2]

Sample activation ($NiNO_3$-CC-OER and $NiFeNO_3$-CC-OER). The as prepared carbon cloth supported $Ni(NO_3)_2$ ($NiNO_3$-CC) and $NiFe(NO_3)_x$ ($NiFeNO_3$-CC) electrodes were activated through chronoamperometry at 1.63 V_{RHE} for at least 30 minutes immediately after being submerged into the 1.0 M aqueous KOH electrolyte. For characterisation, the electrodes were washed with water and dried in air. The electrodes after activation are called $NiNO_3$-CC-OER and $NiFeNO_3$-CC-OER.

_iR_ compensation. The uncompensated resistance (R_u) was determined through impedance spectroscopy with 100 MHz, an amplitude of 10 mV, and at a potential of 1.175 V_{RHE} prior to each measurement and was found to be usually in the range of 1.6-1.8 Ω. The potential was corrected by 90 % of R_u.

Cyclic and linear scan voltammetry. CVs and LSVs were recorded at 5 mV s^{-1} without stirring, if not stated otherwise (30 ml beaker, 3 cm diameter) and _iR_ compensation.

Chronoamperometry and chronopotentiometry. The CA and CP measurements were performed with stirring (200 rpm, stirring bar 1 cm, 30 ml beaker, 3 cm diameter) and an applied _iR_ compensation of 90 % in 1.0 M aqueous KOH. For the long-term chronopotentiometry measurements, the beaker was covered and milli-Q® water was added regularly to keep the electrolyte volume constant. Additionally, the electrolyte was temperature controlled at 25 °C.

Steady-state Tafel analysis. CA measurements for 3 min or until a stable current was reached at each potential were performed to acquire the respective current densities. The Tafel slope was determined according to the Tafel equation $\eta = b \times \log(i) + a$, where η is the overpotential in V, i is the current density in mA cm^{-2}, and b is the Tafel slope in mV dec^{-1}.[3]

Electrochemical oxidation of 5-hydroxymethylfurfural (HMF). The electrocatalytic oxidation of HMF was accomplished in an undivided cell with $NiNO_3$-CC-OER or $NiFeNO_3$-CC-OER as the working electrodes, a

Hg/HgO electrode as the reference electrode, and a platinum wire as the counter electrode. CVs and LSVs at 5 mV s^{-1} were recorded in 15 mL 1.0 M KOH solution containing 50 mM HMF without stirring if not stated otherwise. Steady-state bulk electrolysis was performed under constant potential (1.52 V$_{RHE}$) with stirring (600 rpm) (40 ml beaker, 1 cm stirring bar, 3 cm diameter).

Turnover frequency (TOF). Electrodes with different metal loadings were prepared and activated. Subsequently, CA was conducted at η = 400 mV (1.63 V$_{RHE}$) for each electrode to measure the current density j (mA cm^{-2}). The TOF was calculated from the following equations:

$$TOF = j / [4 \cdot F \cdot n^*] \tag{1}$$

$$n^* = L \cdot [M_{Ni,\%} / M_{Ni,u} + M_{Fe,\%} / M_{Fe,u}] \tag{2}$$

Where F is the Faraday constant (96 485 C mol^{-1}), n^* is the mol of metal per cm^{2,} which was derived from the metal loading (L) in mg per cm² by equation (2), where $M_{M\%}$ is the weight percent of the overall metal loading and M_u is the atomic mass of the respective metal.

Characterisation details

Powder X-ray diffraction. A Panalytical X'Pert PRO diffractometer (Bragg-Brentano geometry, Cu-K$_\alpha$ radiation) was used for powder XRD measurements.

X-ray photoelectron spectroscopy. XPS measurements were carried out using a ThermoScientific K-Alpha+ X-ray photoelectron spectrometer. All samples were analysed using a micro focused, monochromated Al-K$_\alpha$ X-ray source (1486.68 eV; 400 µm spot size). The analyzer had a pass energy of 200 eV (survey), and 50 eV (high-resolution spectra), respectively. Binding energies were calibrated to the C 1s peak at 284.8 eV. To prevent any localized charge build up during analysis the K-Alpha+ charge compensation system was employed at all measurements. The samples were mounted on conductive carbon tape or measured directly from the carbon cloth substrate for Ni 2p, Fe 2p, O 1s, N 1s and K 2p levels with a pass energy 20 eV and step size of 0.1 eV. The binding energies were calibrated relative to the C 1s peak energy position as 285.0 eV. Data analyses were carried out using Casa XPS (Casa Software Ltd.) and the Vision data processing program (Kratos Analytical Ltd.).

Scanning electron microscopy. SEM images were acquired and performed on a ZEISS GeminiSEM500 NanoVP microscope integrated with an energy dispersive X-ray (EDX) detector (Bruker Quantax XFlash®

6|60). For data handling and analysis, the software package EDAX was used. The SEM experiments on the GeminiSEM500 system were performed at the Zentrum für Elektronenmikroskopie (ZELMI) of the TU Berlin.

Characterisation of HMF oxidation products. The oxidation reaction mixture was characterised by ^{1}H NMR spectroscopy in a 400 MHz JEOL NMR and Bruker AV400 instrument. After the reaction, maleic acid was added to the reaction solution as an internal standard, equal to the starting concentration of 5-HMF (typically 50 mM). The ^{1}H NMR sample was prepared by taking a 150 µL aliquot of the reaction mixture solution and 350 µL D_2O solvent. Processing and plotting of the spectra were performed using MestReNova software. A sharp peak at 4.7 ppm appeared for the H_2O from the aqueous reaction mixture and was used as a reference for the chemical shifts of the other proton signals. The chemical shift values of the protons of the organic products were assigned accordingly and compared with reported literature values.[4] The HMF oxidation product (FDCA) was quantified (chemical conversion) by calculating the relative intensity of the proton signals. Chemical conversion and Faradaic efficiency (FE) were calculated using the following equations:

$$\text{Chemical conversion (\%)} = [n_{product} / n_{reactant\ initial\ conc.}] \times 100 \qquad (3)$$

$$\text{FE (\%)} = [n_{product} \cdot n_e \cdot F / (Q)] \times 100 \qquad (4)$$

Where F is the Faraday constant (96 485 C mol^{-1}), n is the mol of reactant quantified from ^{1}H NMR, n_e is the number of electrons needed for the oxidation process (6 for HMF), and Q is the charge (coulombs) passed through the solution.
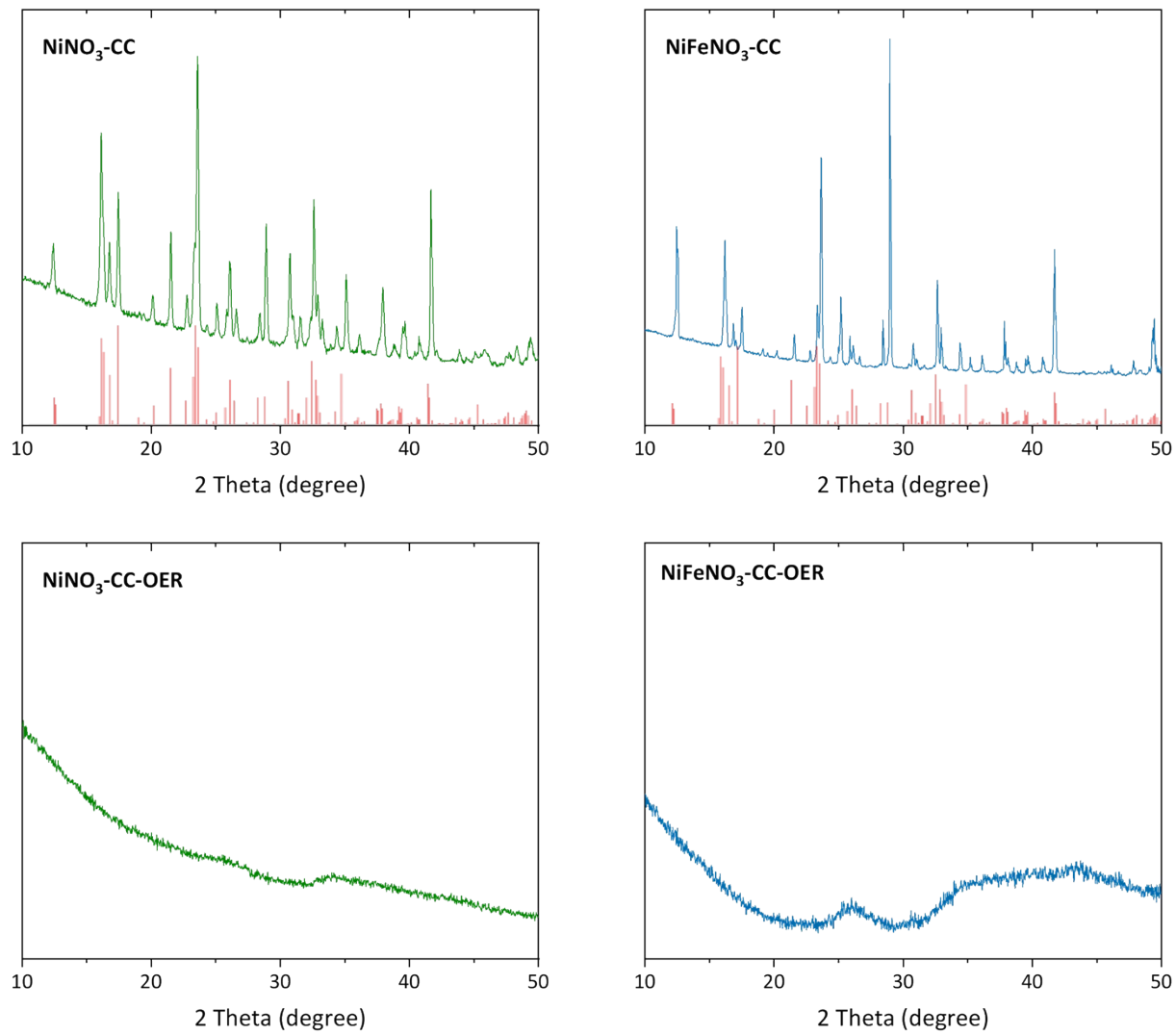
Fig. S1. X-Ray-diffraction (XRD) pattern of the drop-coated nickel(-iron) nitrate on carbon cloth (CC) before (top) and after (bottom) OER ($NiNO_3$-CC(-OER) and $NiFeNO_3$-CC(-OER)).
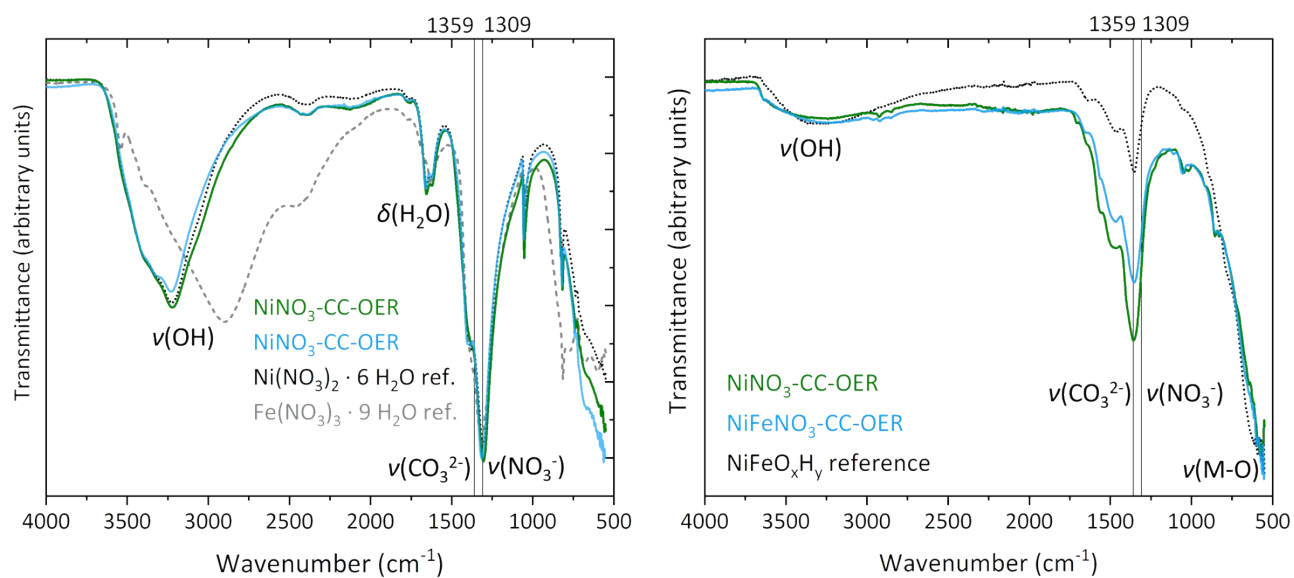
Fig. S2. Infrared spectrum of drop-coated nickel and nickel-iron nitrate. To minimise the interference of the infrared-active carbon cloth with the drop-coated nitrates, we drop-coated the nitrates on a flat inert substrate and scratched them off. The obtained powders were then measured. Nickel nitrate hexahydrate and iron nitrate nonahydrate were additionally measured as references. The spectra of the samples match well with those of nickel nitrate hexahydrate.
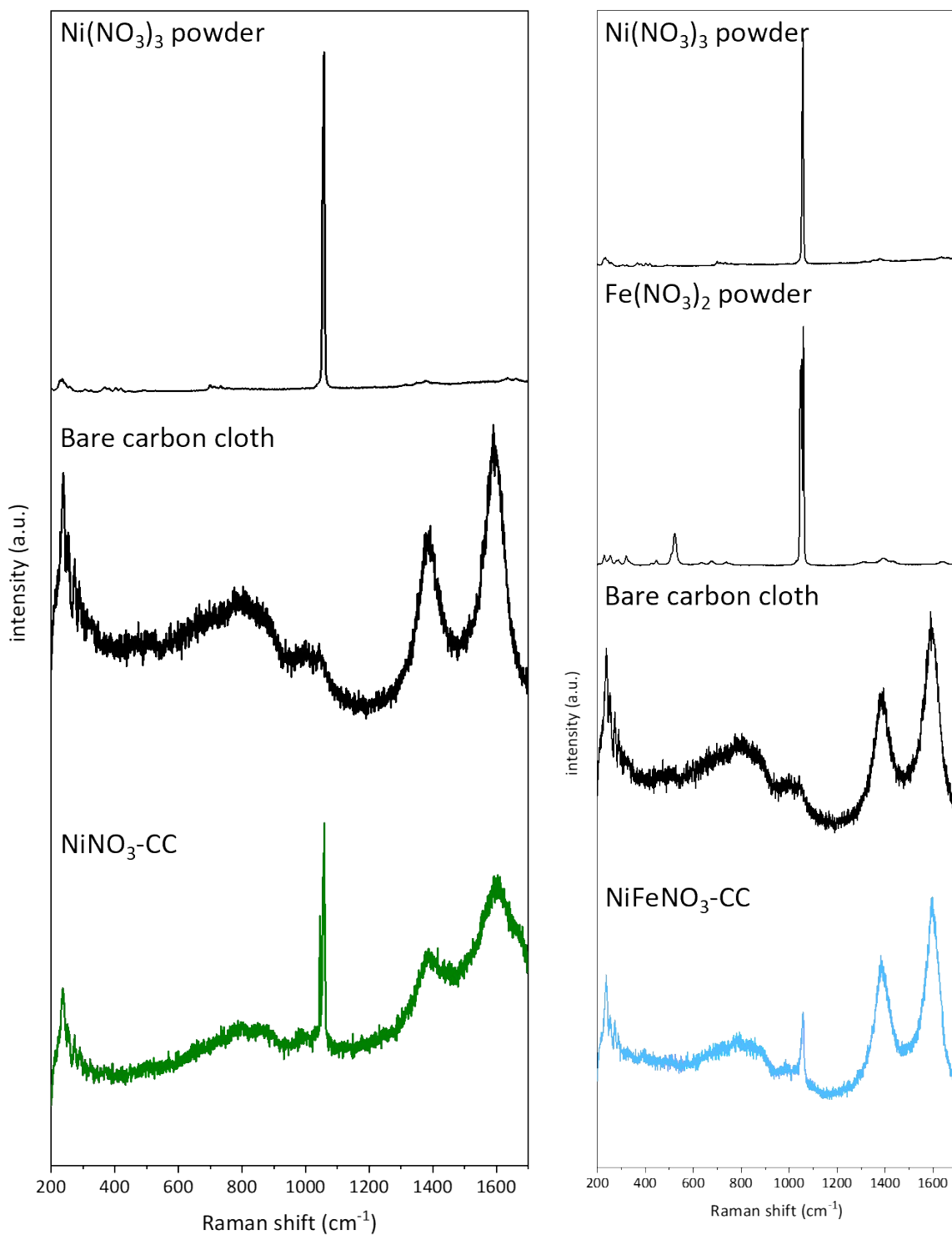
Fig. S3. Raman spectra of Ni(NO$_3$)$_3$ and Fe(NO$_3$)$_2$ powder, bare carbon cloth and as prepared NiNO$_3$-CC and NiFeNO$_3$-CC electrodes.
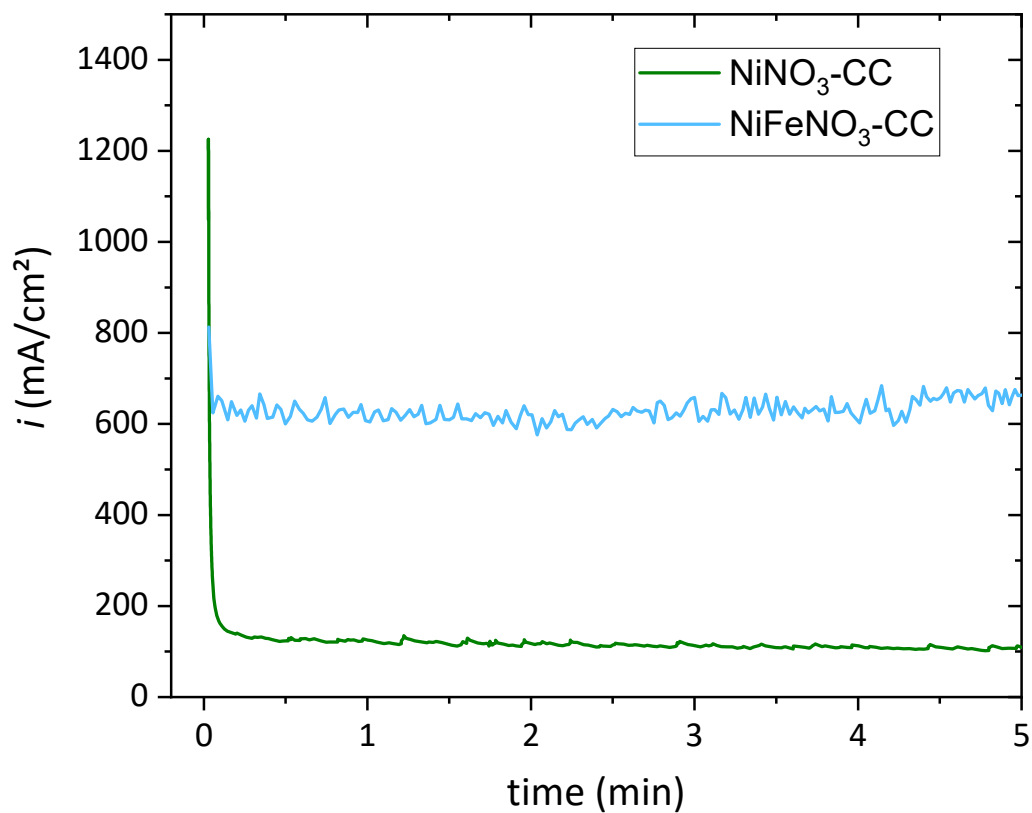
Fig. S4. Current response of NiNO$_3$-CC and NiFeNO$_3$-CC for Chronoamperometry at 1.63 V$_{RHE}$ in 1M KOH electrolyte. The peak in current at the start of the measurement is assigned to the catalyst oxidation into oxyhydroxides. The potential was kept stable for 30 minutes to ensure full conversion and a steady state of the electrode.
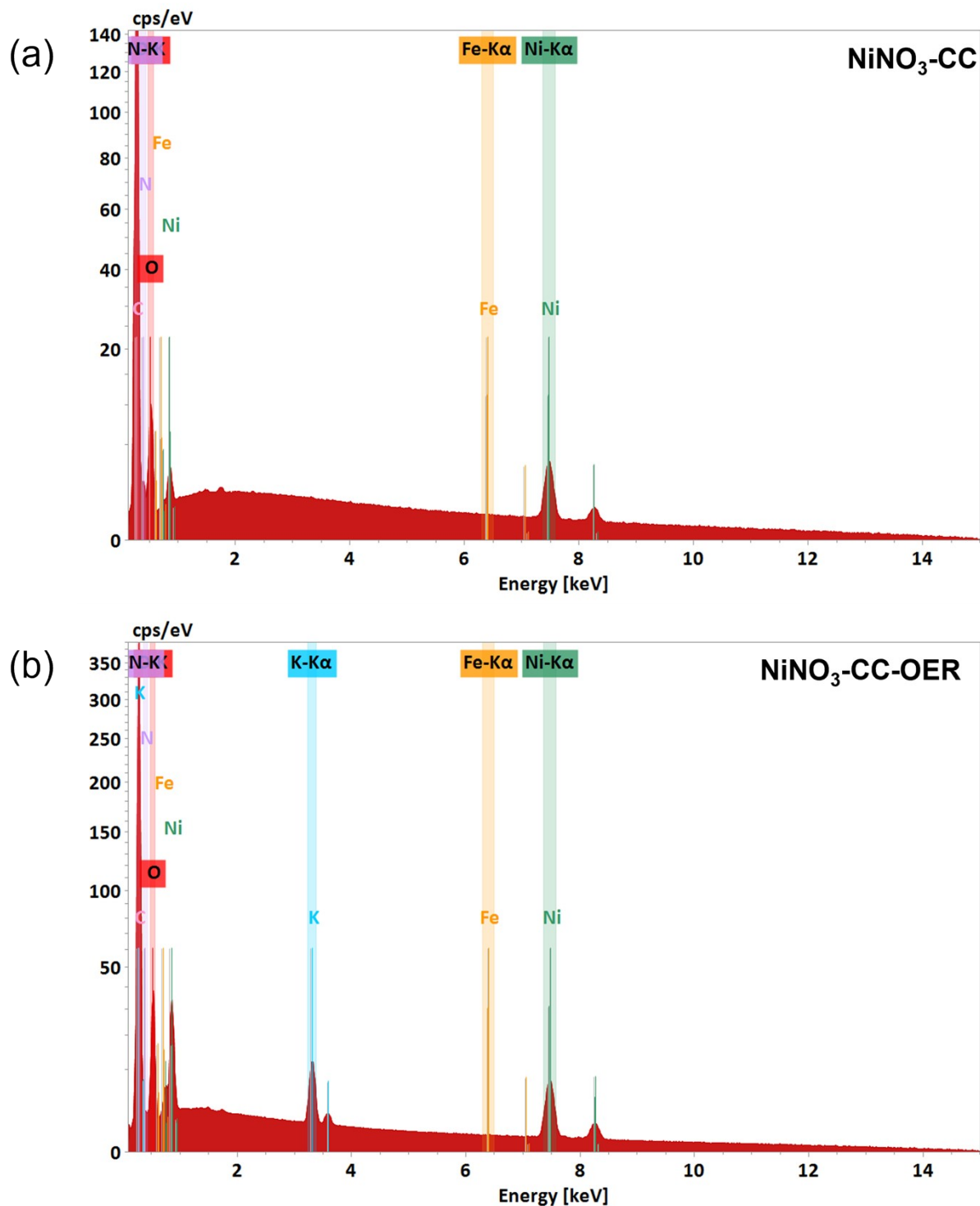
Fig. S5 EDX analysis of a) NiNO$_3$-CC and b) NiNO$_3$-CC-OER electrodes obtained from SEM measurements. The spectra show the presence of Ni, C, and O, while no iron peak is visible. No clear assignment of N can be done due to the large C peak. After OER, the sample contains potassium. As reported previously for the OER of nickel oxyhydroxides in aqueous potassium hydroxide, this potassium is most likely intercalated into the layer nickel(iron) oxyhydroxide structure.[5–7]
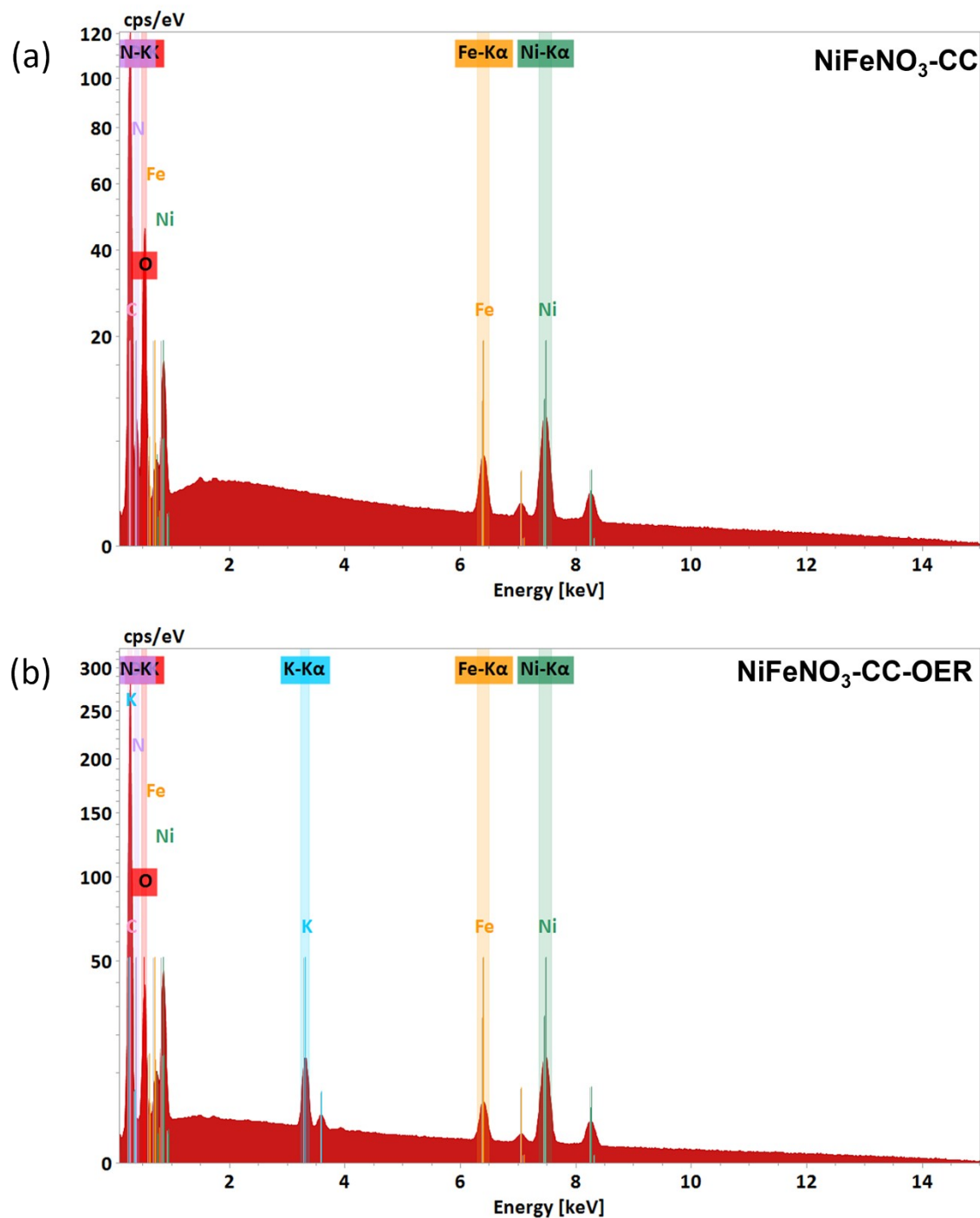
Fig. S6 EDX analysis of a) NiFeNO$_3$-CC and b) NiFeNO$_3$-CC-OER electrodes obtained from SEM measurements. The spectra show the presence of Ni, Fe, C, and O. No clear assignment of N can be done due to the large C peak. After OER, the sample contains potassium. As reported previously for the OER of nickel oxyhydroxides in aqueous potassium hydroxide, this potassium is most likely intercalated into the layer nickel(iron) oxyhydroxide structure.[5–7]
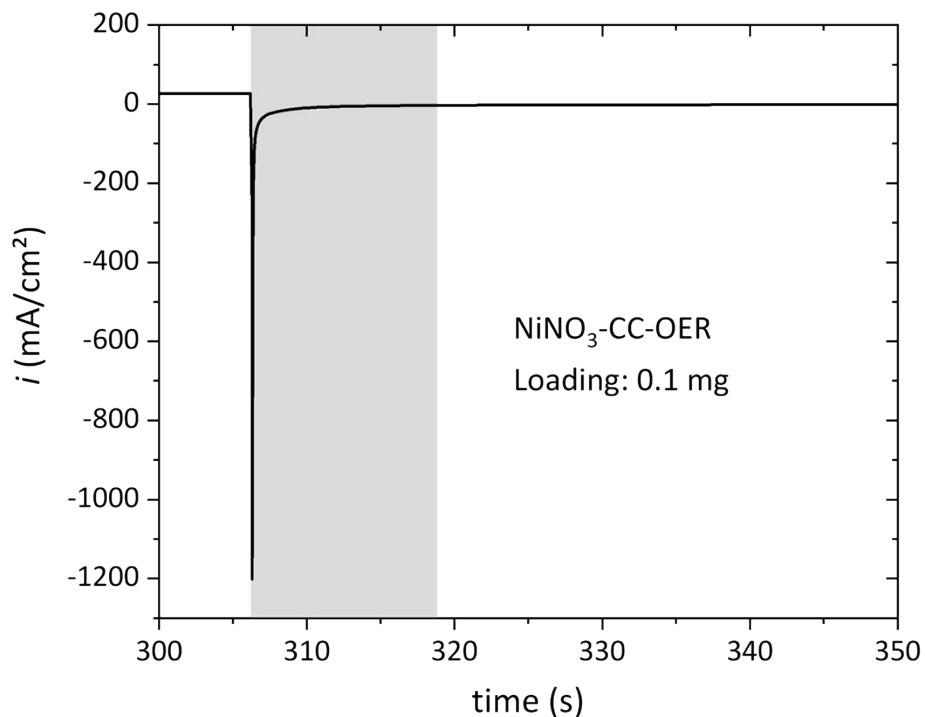
Metal loading	NiNO₃-CC-OER Portion of redox active sites	NiFeNO₃-CC-OER Portion of redox active sites
0.01 mg	>100 %	>100 %
0.015 mg	>100 %	>100 %
0.02 mg	>100 %	>100 %
0.025	>100 %	>100 %
0.05 mg	76 %	76 %
0.1 mg	65 %	48 %
0.25 mg	48 %	34 %
0.5 mg	36 %	23 %
1.0 mg	41 %	17 %
2.0 mg	34 %	12 %
3.0 mg	32 %	9 %

$$Redox\,active\,sites\,[mol] = \frac{1}{F} * \int_{t_1}^{t_2} I(t)dt$$

Fig. S7. Determination of the number of redox active sites by a potential step method.[4,8,9] In this method, an OER potential is applied for 5 minutes to ensure that all metal sites are oxidized. Then, a potential of below the redox peak (herein 1.0 V_{RHE}, see Fig. 3b for a CV) is applied that lead to the reduction of these sites. At the top such an example for such a measurement is shown. The transferred reductive charge can be used to determine the number of redox active sites by dividing it by the Faraday constant and considering that around 1.6 electrons are transferred per nickel (see reference [4] for a discussion). For very low loadings, this method overestimated the number of redox active sites as also other processes can contribute to the measured reductive current (e.g., the double layer capacitance of the carbon cloth or other reductive processes of the carbon cloth surface). This data should be treated as a qualitative trend. Furthermore, the addition of iron changes the redox activity of nickel.[4,10] Thus, the data for the monometallic nickel and the bimetallic nickel iron sample should not be compared directly.
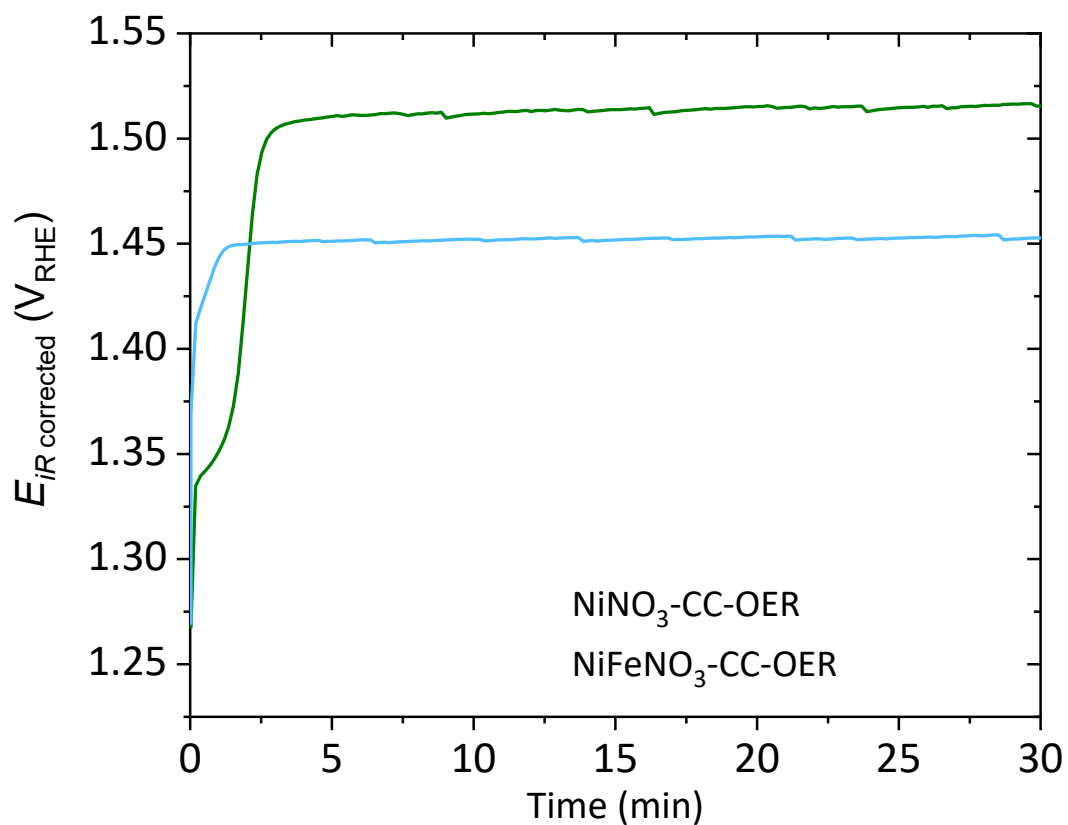
Fig. S8. CP without stirring at 10 mA cm^{-2} to reliably determine the OER overpotential. NiNO$_3$-CC-OER (green curve) shows an overpotential of 290 mV, while NiFeNO$_3$-CC-OER (blue) achieves the desired current density at only 220 mV. Both results are consistent with the overpotential determined from the back scan of the CVs shown in the main text in Fig. 3 b).

Table S1: Performance comparison

Catalyst	Substrate	Stability (h)	η_{10} (mV)	Reference
$Ni(NO_3)_3$	**CC**	**40**	**280**	**This work**
$NiFe(NO_3)_x$	**CC**	**40**	**220**	**This work**
NiGe	NF	168	245	*Angew. Chem., Int. Ed.* **2021**, 133, 4690
NiFeOOH	NiFe	2	240	*ChemSusChem* **2019**, 12, 1966
NiO_x-Fe	NF	18	215	*ACS Cent. Sci.* **2019**, 5, 558
NiFe LDH	NF	13	300	*Nat. Commun.* **2014**, 5, 4477
$Ni_3Fe_{0.5}V_{0.5}$	CFP	60	250	*Nat. Commun.* **2018**, 9, 2885
NiFe LDH	GC	1	230	*ACS Nano* **2015**, 9, 1977
Ni_2P	NF	12	240	*ACS Catal.* **2017**, 7, 103
$Ni_{12}P_5$	NF	12	260	*Am. Chem. Soc.* **2014**, 136, 13118
NiFe LDH	HOPG	5	260	*Am. Chem. Soc.* **2014**, 136, 13118
Ni_3S_2	NF	200	260	*J. Am. Chem. Soc.* **2015**, 137, 14023
NiFe-LDH	NF	3	240	*Electrochim. Acta* **2017**, 225, 303
Ni_2P	FTO	16	330	*ACS Catal.* **2017**, 7, 103
$Ni_{12}P_5$	FTO	16	295	*ACS Catal.* **2017**, 7, 103
$FeNiO_xH_y$	NF	50	206	*ChemSusChem* **2018**, 11, 1761
$CuO@NiFeOH_x$	Cu	16	230	*Electrochim. Acta* **2019**, 318, 695
NiFe-MOF	CFP	100	275	*Small* **2019**, 15, 1903410
NiFe-LDH	CW	-	260	*Nanotechnology* **2019**, 30, 32
NiFe-LDH	NW	1.5	300	*ACS Appl. Energ. Mater.* **2019**, 2, 5465
NiFe alloy	GC	2	298	*Catal. Today* **2020**, 352, 27
NiFe-MOF	GC	5.5	230	*ACS Catal.* **2020**, 10, 5691
NiFeTiOOH	GC	24	400	*ACS Catal.* **2020**, 10, 4879
NiFeCo-LDH	CFP	10	288	*ACS Catal.* **2020**, 10, 5179
NiFe alloy	GC	20	246	*ACS Appl. Energ. Mater.* **2020**, 3, 3966
CNS-NiFe	Cu_2O/Cu	24	248	*Catal. Lett.* **2020**, 150, 3049
NiFe-LDH	CB	6	236	*Catalysts* **2020**, 10, 431
$NiFe/CoFe_2O_4/Co_3S_4$	CFP	48	233	*Sustain. Energ. Fuels* **2020**, 4, 1933
$Ni(OH)_2(CO_3)$-Fe^{2+}	NF	36	277	*Inorg. Chem. Comm.* **2020**, 114, 107851
$NiFeNiFe_2O_4$	NF	15	316	*J. Phys. Chem. Solids* **2020**, 139, 109325
$NiFe_xSn@NiFe(OH)_x$	CFC	11	260	*Adv. Sci.* **2020**, 7, 1903777
Co-NiFe-LDH	GC	20	278	*Int. J. Hydrogen Energy* **2020**, 45, 9368
$NiFe(Co_3)^{2-}$-LDH	NF	20	228	*Chemistryselect* **2020**, 5, 3062

NiFe	NF	30	270	*Appl. Sur. Sci.* **2020**, 503
NiFe$_2$O4/NFM	Fe wire	10	234	*J. Alloys Comp.* **2020**, 813, 152219
NiFe15	NiFe sponge	24	280	*Chemistryselect* **2020**, 5, 1385
NiO/C@NiFe-LDH		10	299	*J. Electrochem. Soc.* **2020**, 167, 037555
NiFe-LDH@Ni$_3$S$_2$	NF	6	271	*Nanotechnology* **2019**, 30, 484001
NiFe-HC	GC	12	330	*Sci Rep* **2019**, 9, 11
Ni$_1$Fe$_{10}$-LDH@Ni$_3$S$_2$	NF	12	230	*Electrochim. Acta* **2019**, 318, 42
NiFeS2	GC	24	230	*J. Mater. Chem. A* **2017**, 5, 4335
NiFeS	GC	6	286	*Small* **2017**, 13
Ni0.7Fe0.3S2+y	NF	24	210	*Sustain. Energy Fuels* **2018**, 2, 1561
Ni0.7Fe0.3S2	NF	14	198	*J. Mater. Chem. A* **2017**, 5, 15838
NixFe1-xSe2	GC	24	195	*Nat. Commun.* **2016**, 7, 12324
NiFe LDH	GC	8	280	*Nano Research* **2018**, *11,* 1883
FeSe$_2$	GC	70	330	*Nano Energy* **2017**, *31,* 90

GC = glassy carbon, CFP = carbon fiber paper, Au = gold, CC =carbon cloth, FTO = fluorine doped tin oxide, HOPG = highly-ordered pyrolytic graphite, NF = nickel foam, CW= carbon wire; CB = carbon black
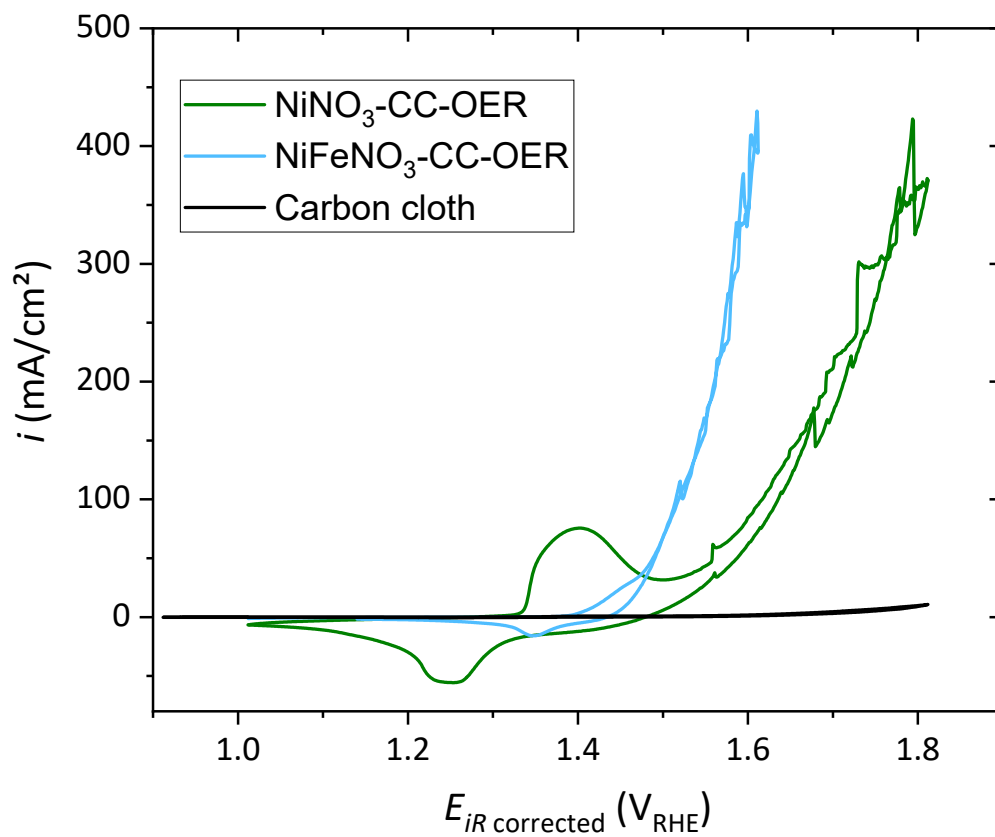
Fig. S9. CV of acid treated bare carbon cloth in 1.0 M KOH compared to NiNO$_3$-CC-OER and NiFeNO$_3$-CC-OER.
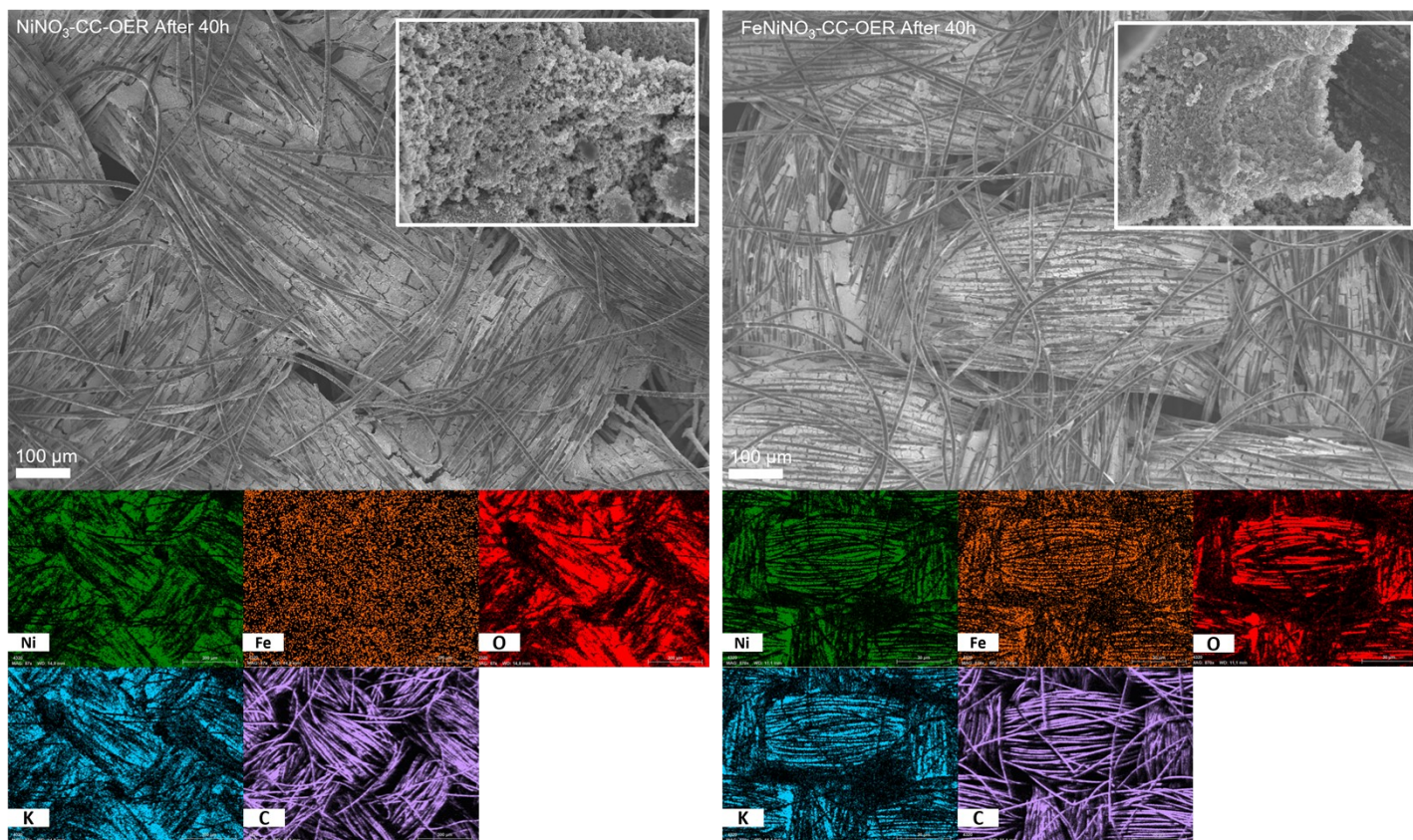
Fig. S10. SEM pictures and EDX mappings of $NiNO_3$-CC-OER and $NiFeNO_3$-CC-OER after the 40h stability test. The pictures indicate that homogeneous distribution of Nickel (and Iron for $NiFeNO_3$-CC-OER) and Oxygen is retained throughout the measurement without a visible change in morphology when compared to the SEM pictures after avtivation in Fig 2.
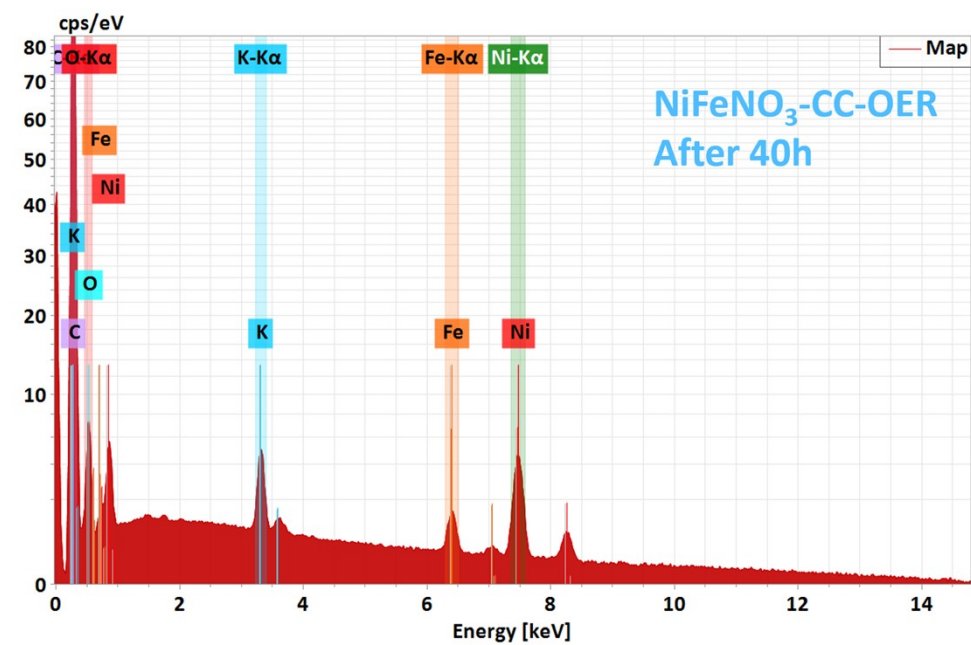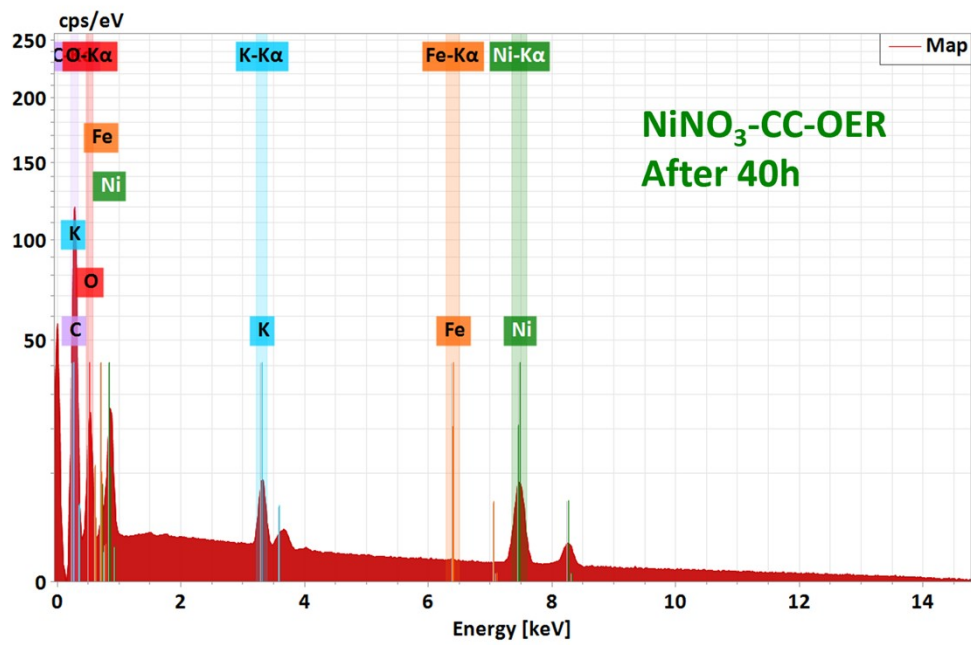
Fig. S11. EDX spectra of NiNO$_3$-CC-OER and NiFeNO$_3$-CC-OER after the 40h stability test.
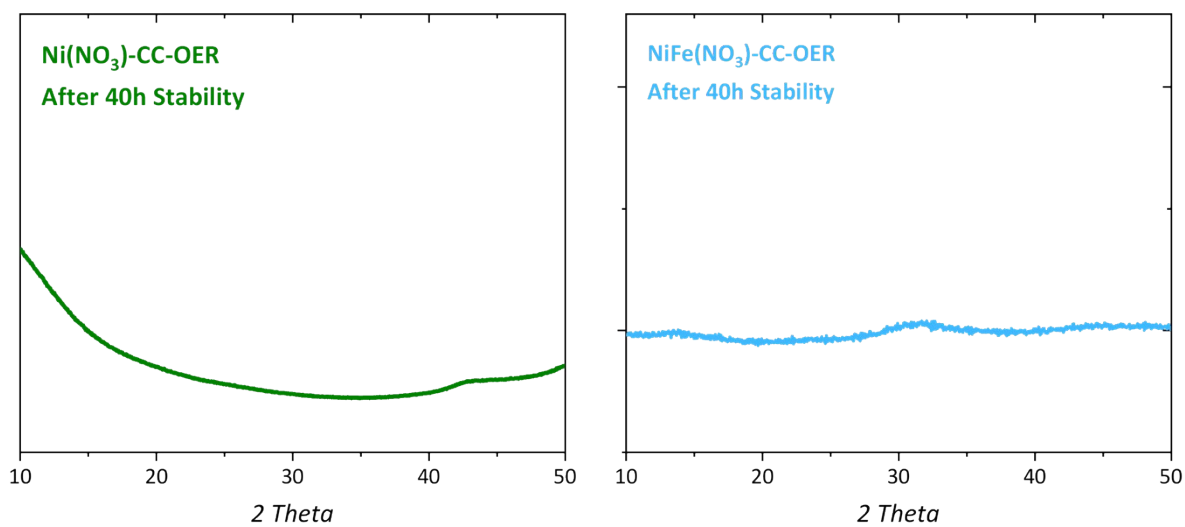
Fig. S12. . X-Ray-diffraction (XRD) pattern of both electrodes after 40h stability test. No visible peaks indicate that the amorphous structure measured after activation is retained.
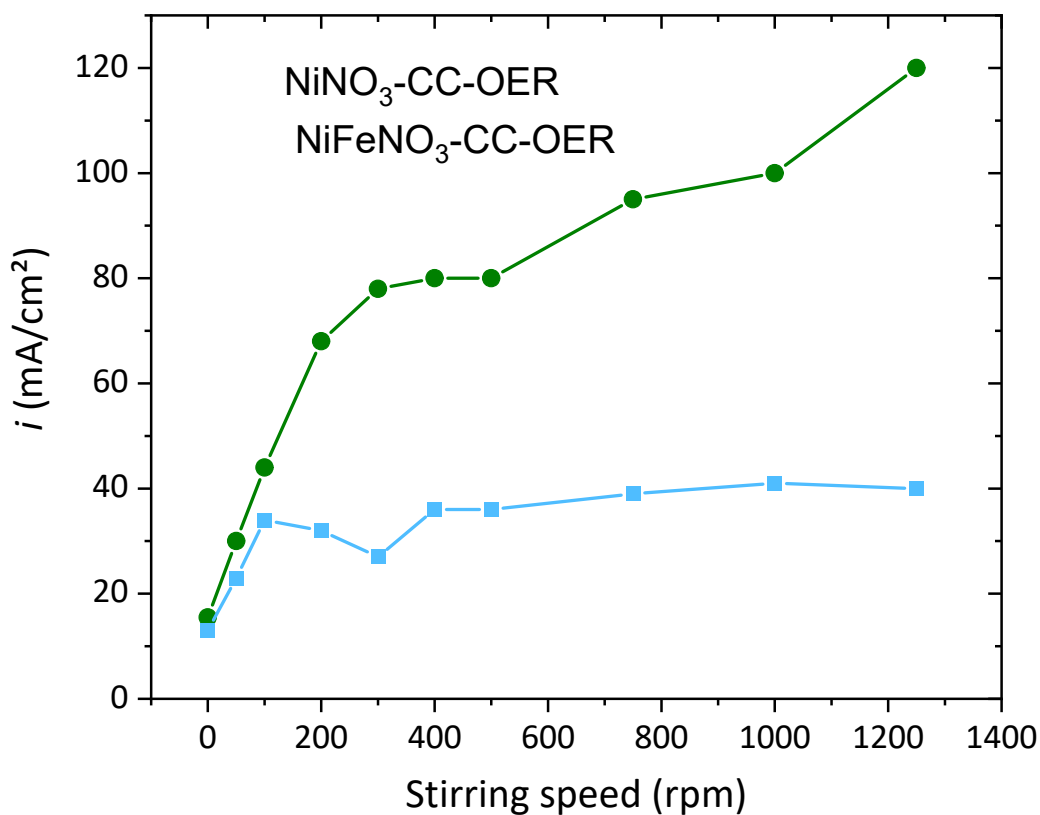
Fig. S13. Influence of stirring speed on the current density during HMF conversion. The data was obtained from CP measurements with fresh 50 mM HMF in 1.0 M KOH at 1.41 V_{RHE}. While the current density constantly increases with the stirring speed for $NiNO_3$-CC-OER (green)reaching current densities of up to 120 mA cm^{-2}, $NiFeNO_3$-CC-OER (blue) quickly reaches a plateau at 200 rpm stirring speed only achieving 40 mA cm^{-2}. This indicates that transport limitations are not the reason for the weak catalytic performance of $NiFeNO_3$-CC-OER compared to $NiNO_3$-CC-OER, which seems to be catalytical highly active but limited by mass transport.

50 mM HMF
In 1.0 M KOH with internal standard
Before reaction

7.41   6.52   5.93   4.58
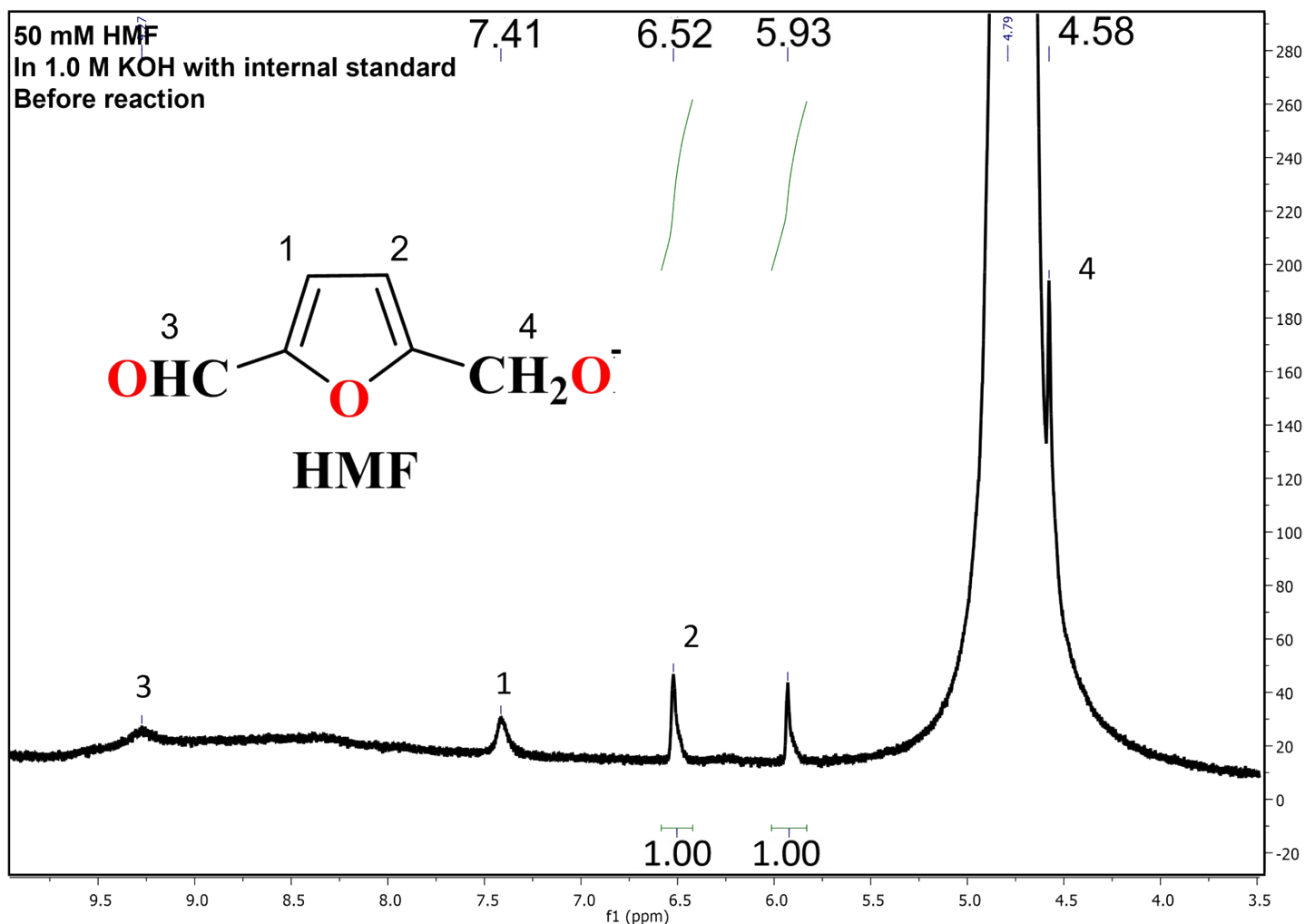
Fig. S14. ^{1}H-NMR spectrum of the reaction mixture before conversion. The strong singlet peak at 4.79 of H_2O was used to calibrate the spectrum. The peak at 5.92 ppm corresponds to the internal standard (maleic acid). The broad singlet at 9.27 ppm can be assigned to the aldehyde (-CHO) group in HMF, while the peaks at 7.41 ppm and 6.52 ppm belong to the furan ring protons (-H) as pictured above. The singlet at 4.58 overlapped by the water peak corresponds to the two protons of the alcohol-linked carbon atom.
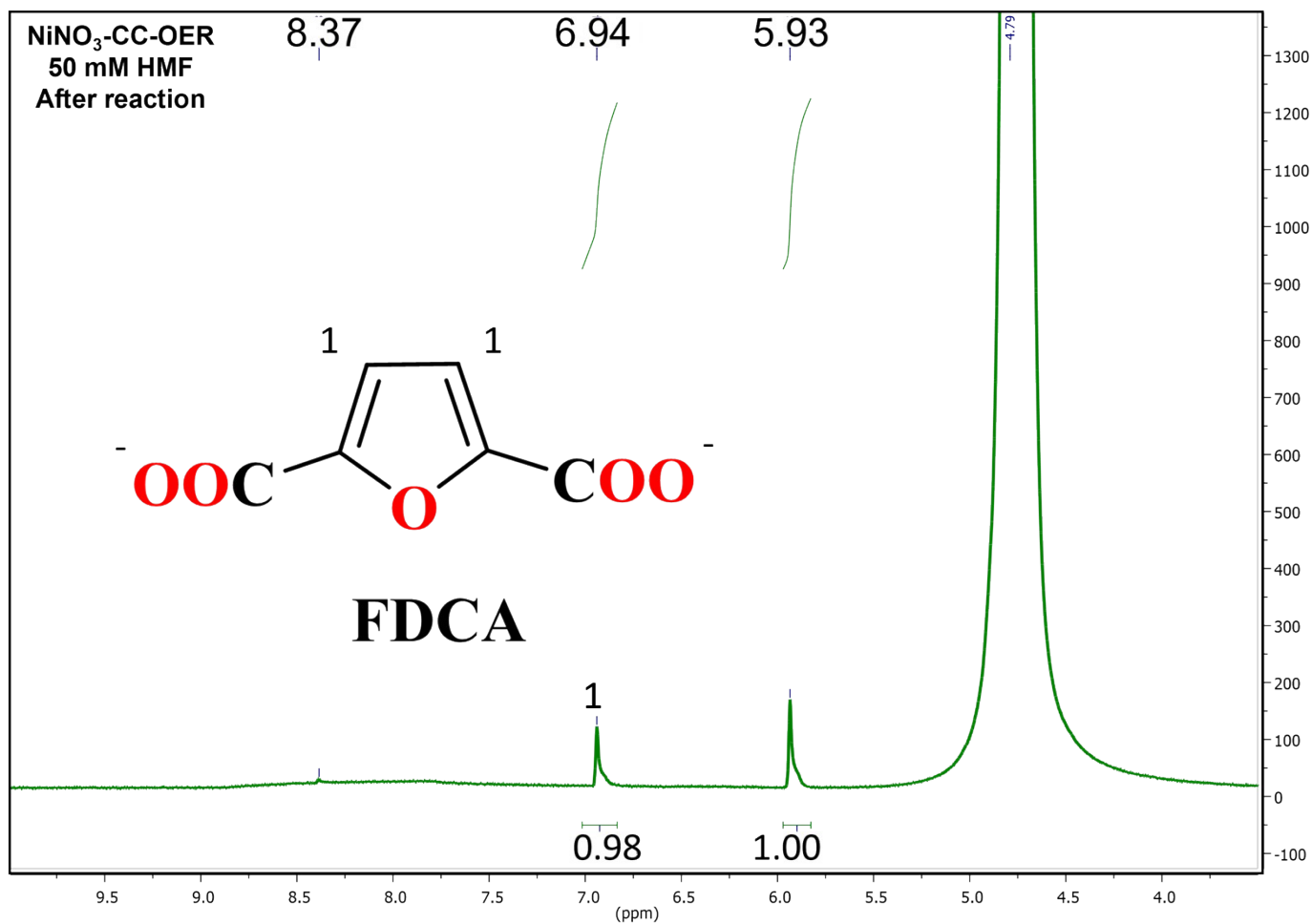
Fig. S15. ^{1}H-NMR spectrum of the reaction mixture after conversion using NiNO$_3$-CC-OER as the catalyst. The strong singlet peak at 4.79 of H$_2$O was used to calibrate the spectrum. The peak at 5.93 ppm corresponds to the internal standard (maleic acid) used for quantification of FDCA. The singlet peak at 6.94 ppm is related to the CH protons of the Furan ring in FDCA. Integration reveals 98 % conversion to FDCA. The minor peak at 8.38 ppm is connected to the decomposition of HMF in basic media, which has been reported before.[11]
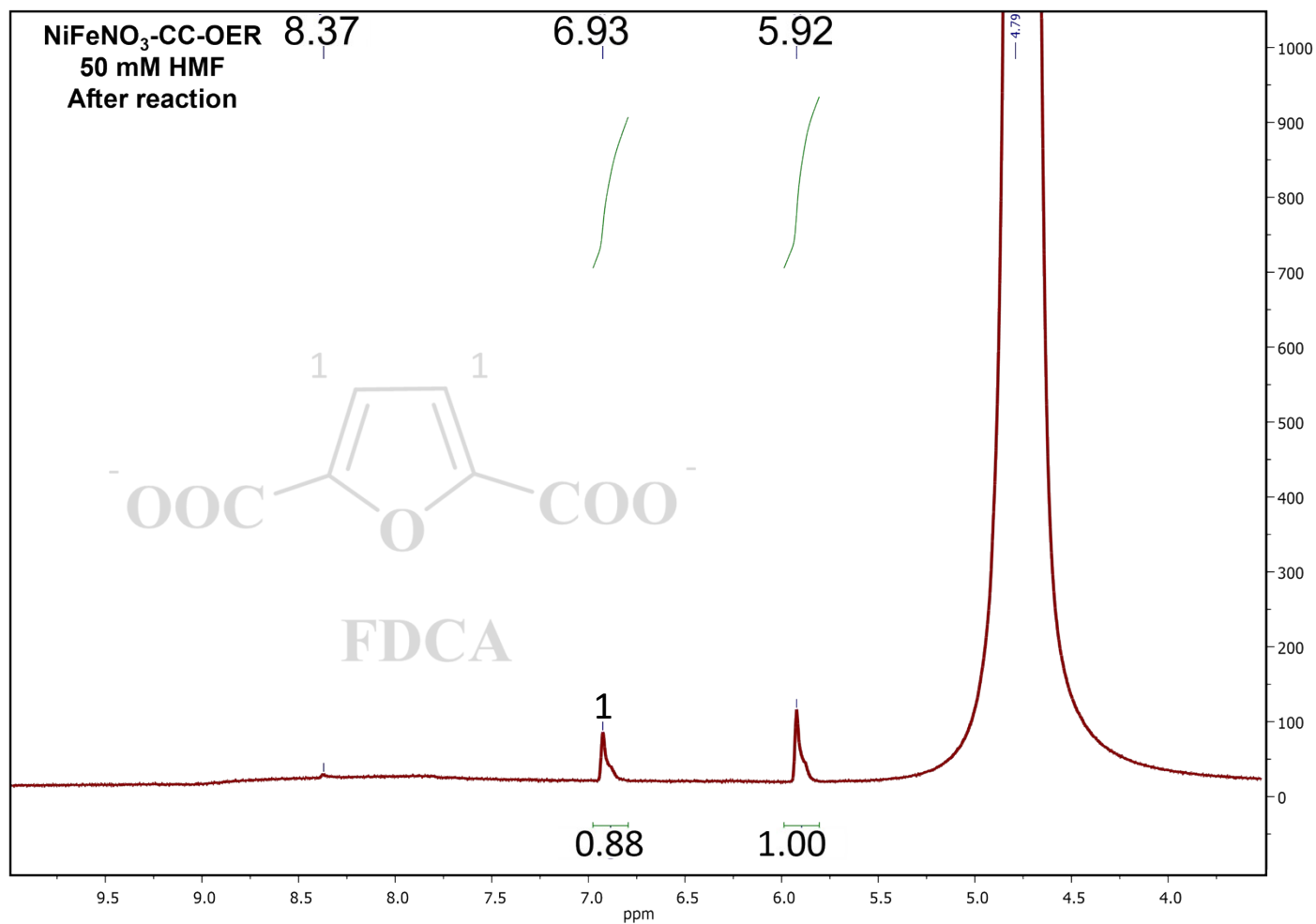
Fig. S16. ^{1}H-NMR spectrum of the reaction mixture after conversion using NiFeNO$_3$-CC-OER as the catalyst. The strong singlet peak at 4.79 of H$_2$O was used to calibrate the spectrum. The peak at 5.92 ppm corresponds to the internal standard (maleic acid) used for quantification of FDCA. The singlet peak at 6.93 ppm is related to the CH protons of the Furan ring in FDCA. Integration reveals 88 % conversion to FDCA. The minor peak at 8.38 ppm is connected to the decomposition of HMF in basic media, which has been reported before.[11]

References

1 J. N. Hausmann, B. Traynor, R. J. Myers, M. Driess and P. W. Menezes, *ACS Energy Letters*, 2021, **6**, 3567–3571.

2 S. Niu, S. Li, Y. Du, X. Han and P. Xu, *ACS Energy Letters*, 2020, **5**, 1083–1087.

3 S. Anantharaj, S. Noda, M. Driess and P. W. Menezes, *ACS Energy Letters*, 2021, **6**, 1607–1611.

4 J. N. Hausmann, P. V. Menezes, G. Vijaykumar, K. Laun, T. Diemant, I. Zebger, T. Jacob, M. Driess and P. W. Menezes, *Advanced Energy Materials*, 2022, 2202098.

5 J. N. W. Hausmann and P. W. Menezes, *Angewandte Chemie International Edition*, 2022, **61**, e202207279.

6 F. Dionigi, Z. Zeng, I. Sinev, T. Merzdorf, S. Deshpande, M. B. Lopez, S. Kunze, I. Zegkinoglou, H. Sarodnik, D. Fan, A. Bergmann, J. Drnec, J. F. de Araujo, M. Gliech, D. Teschner, J. Zhu, W.-X. Li, J. Greeley, B. R. Cuenya and P. Strasser, *Nature Communications*, 2020, **11**, 2522.

7 B. Dasgupta, J. N. Hausmann, R. Beltrán-Suito, S. Kalra, K. Laun, I. Zebger, M. Driess and P. W. Menezes, *Small*, 2023, 2301258.

8 H. N. Nong, L. J. Falling, A. Bergmann, M. Klingenhof, H. P. Tran, C. Spöri, R. Mom, J. Timoshenko, G. Zichittella, A. Knop-Gericke, S. Piccinin, J. Pérez-Ramírez, B. R. Cuenya, R. Schlögl, P. Strasser, D. Teschner and T. E. Jones, *Nature*, 2020, **587**, 408–413.

9 R. D. L. Smith, C. Pasquini, S. Loos, P. Chernev, K. Klingan, P. Kubella, M. R. Mohammadi, D. Gonzalez-Flores and H. Dau, *Nature Communications*, 2017, **8**, 2022.

10 D. A. Corrigan, *Journal of The Electrochemical Society*, 1987, **134**, 377.

11 D. H. Nam, B. J. Taitt, K. S. Choi, ACS Catal. 2018, 8, 1197.